

## Elucidating the mechanism of step emulsification

Andrea Montessori,<sup>1,2</sup> Marco Lauricella,<sup>1</sup> Sauro Succi,<sup>1,3,4</sup> Elad Stolovicki,<sup>5</sup> and David Weitz<sup>5,6</sup>

<sup>1</sup>*Istituto per le Applicazioni del Calcolo CNR, via dei Taurini 19, 00185, Rome, Italy*

<sup>2</sup>*Department of Engineering, University of Rome “Roma Tre,” Via della Vasca Navale 79, 00141 Rome, Italy*

<sup>3</sup>*Center for Life Nanoscience at la Sapienza, Istituto Italiano di Tecnologia, viale Regina Elena 295, I/00161, Rome, Italy*

<sup>4</sup>*Institute for Applied Computational Science, John A. Paulson School of Engineering and Applied Sciences, Harvard University, Cambridge, Massachusetts 02138, USA*

<sup>5</sup>*School of Engineering and Applied Sciences, Harvard University, McKay 517 Cambridge, Massachusetts 02138, USA*

<sup>6</sup>*Department of Physics, and School of Engineering and Applied Sciences, Harvard University, Pierce 231, 29 Oxford Street, Cambridge, Massachusetts 02138, USA*



(Received 22 March 2018; revised manuscript received 14 May 2018; published 30 July 2018)

Three-dimensional, time-dependent direct simulations of step emulsification microdevices highlight two essential mechanisms for droplet formation: first, the onset of an adverse pressure gradient driving a backflow of the continuous phase from the external reservoir to the microchannel, and second, the striction of the flowing jet which leads to its subsequent rupture. It is also shown that such a rupture is delayed and eventually suppressed by increasing the flow speed of the dispersed phase within the channel, due to the stabilizing effect of dynamic pressure. This suggests a new criterion for dripping-jetting transition, based on local values of the capillary and Weber numbers.

DOI: [10.1103/PhysRevFluids.3.072202](https://doi.org/10.1103/PhysRevFluids.3.072202)

Step emulsification (SE) has captured significant interest in the recent years as a viable microfluidic technique for the controlled production of liquid droplets [1,2]. Among others, one of the main appeals of the SE technique is the prospect of producing large volume rates of the dispersed phase, which are out of reach for previous techniques, such as flow focusers [3–6].

The basic idea behind SE is to exploit the pressure drop due to a sudden channel expansion (step) to induce the pinch-off of the dispersed phase, leading to droplet formation [7]. Albeit conceptually straightforward, the details of the process depend on a number of physical and geometrical parameters, primarily the capillary number  $Ca$  and the aspect ratio  $h/w$  of the height versus width of the microchannel cross section (see Fig. 1). Such parameters dictate the shape of the droplet and the transition between the dripping and the jetting regimes [7–9]. Although of primary importance, the capillary number (viscous dissipation/surface tension) does not capture the full picture and needs to be complemented by other dimensionless groups, namely the Weber number (inertia/surface tension), and/or Reynolds numbers (inertia/viscous dissipation).

Despite major technological advances, the theoretical description and the numerical simulation of microchannel emulsification is still under development.

In this Rapid Communication, we present direct numerical simulations of the fully three-dimensional, time-dependent Navier-Stokes equations for a specific step-emulsification microdevice, in order to elucidate the basic fluid phenomena underpinning the step-emulsification process. The simulations highlight two essential mechanisms: (i) the backflow of the continuous phase from the external reservoir to the confined microchannel, driven by an adverse pressure gradient, and (ii) the resulting striction of the flowing jet within the channel and its subsequent rupture. It is also shown

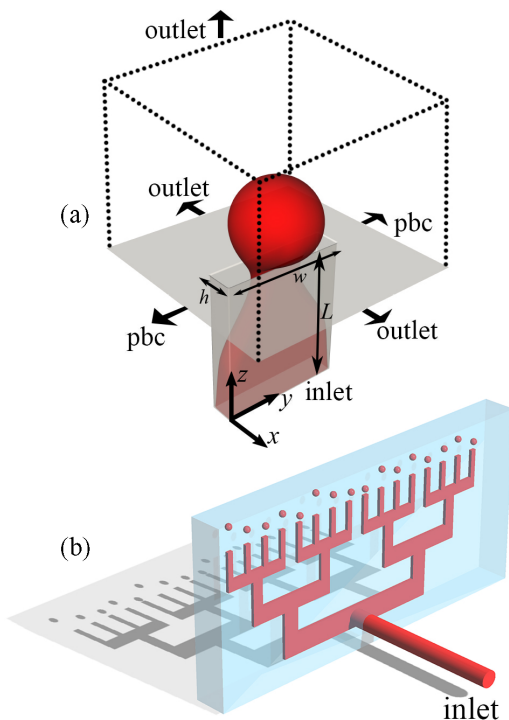


FIG. 1. Sketch of the nozzle geometry in the simulation box, along with the imposed boundary conditions [top panel (a)]. The adopted conditions reproduce a periodic array of independent nozzles, which is consistent with the geometry of the volcano device [bottom panel (b)]. Here, the dispersed phase (red) is pumped through the device, forming monodisperse drops in a reservoir containing a continuous immiscible phase (cyan).

that such a rupture is delayed or even suppressed upon increasing the flow speed of the dispersed phase within the channel, due to the stabilizing effect of dynamic pressure.

In order to simulate the droplet breakup in a recently proposed class of step emulsification devices [2,8,10], we solve the multicomponent Navier-Stokes equations, using an extensions of the lattice Boltzmann method [11–17]. See the Supplemental Material [18]. The device, made of polydimethylsiloxane (PDMS), is used for producing water in oil emulsions and a sketch is reported in Fig. 1. The water flows through the device inlet and splits into hundreds of step-emulsifier nozzles with rectangular cross sections. The PDMS device is submerged in quiescent oil, the continuous phase, with the nozzles pointing upward. The dispersed phase (water) is then pumped through the device and forms monodisperse drops, whose sizes are proportional to the nozzle height ( $h$ ). We wish to point out that, with the device submerged in quiescent oil, there is no net flow of the continuous phase; this in contrast with the emulsification system employed in Ref. [22]. In this work, we simulate a single nozzle out of the full device, using periodic boundary conditions along cross-flow directions, in order to mimic the effect of neighboring nozzles. At the inlet, we impose uniform velocity profiles, while a zero gradient approximation is applied at the outlet. The ratio between the kinematic viscosities of the dispersed and the continuous phase is fixed to  $\sim 1.2$ , as in Refs. [8]<sup>1</sup> and [23–26].

<sup>1</sup>We performed additional simulations in which the same range of capillary numbers was spanned by changing the viscosity  $\nu$  and/or the surface tension  $\sigma$ . The simulation results show that the transition from dripping to jetting occurs almost at the same critical capillary number, corresponding to lower flow rates as the viscosity of the inner phase is increased.

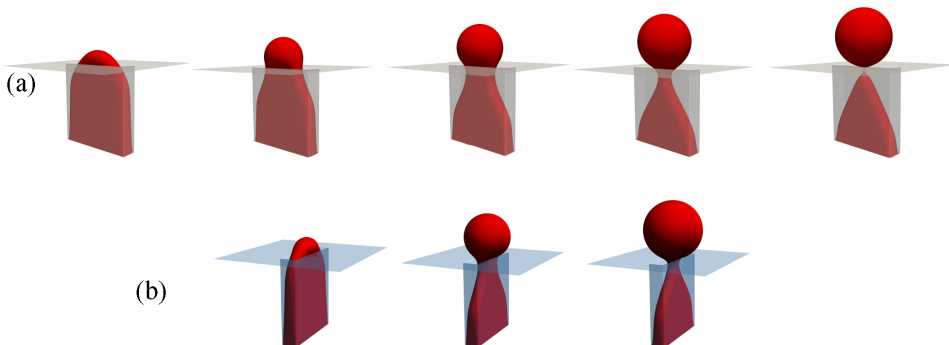


FIG. 2. (a) Sequence of the break process in the dripping regime in a step emulsification nozzle. The dispersed phase (water) is pumped through the device and forms monodisperse drops whose sizes are proportional to the nozzle height. (b) Sequence of the step emulsifier in the jetting regime.

First, we perform a comparison with the experiments reported in Ref. [8], by investigating the effect of the main nondimensional parameters, i.e., the capillary number ( $Ca = \rho U \nu / \sigma$ ) and the Weber number ( $We = \rho U^2 L / \sigma$ ), where  $U$  is the velocity of the dispersed phase at the inlet,  $\rho$  is the density of the dispersed phase,  $L$  is a characteristic length defined as  $\sqrt{wh}$  (see Fig. 1),  $\sigma$  is the oil-water surface tension, and  $\nu$  is the kinematic viscosity of the dispersed phase.

In our simulations, the dispersed phase flows through nozzles with a rectangular cross section of  $135 \times 700 \mu\text{m}^2$  and length  $L = 810 \mu\text{m}$ , with a characteristic nozzle aspect ratio  $h/w = 1/5$ , with  $h$  and  $w$  being the height and the width of the microchannel, respectively. Experiments show that the droplet sizes are nearly independent of the flow rate over an extended range (between 12 and 70 mL/min,  $0.002 < Ca < 0.014$ ) with an average drop diameter of  $d = 567 \pm 6 \mu\text{m}$ . In this range of flow rates, thus for capillary numbers in the range  $\mathcal{O}(10^{-3}) \div \mathcal{O}(10^{-2})$ , the step emulsifier has been shown to operate in the dripping regime, while for larger flow rates, i.e., for capillary numbers larger than a critical value, a transition from dripping to jetting regime occurs, which is characterized by the production of much larger and polydisperse droplets [2, 10].

The dripping-jetting transition occurs whenever the droplet does not break up anymore and starts “ballooning” (i.e., above a critical capillary number the newborn droplet grows larger; see Fig. 2). The simulations exhibit a satisfactory agreement with the experimental results, as shown in Fig. 3. First, in the dripping region ( $0.002 < Ca < 0.0125$ ), the average droplet diameter is  $d \sim 540 \mu\text{m}$  ( $d/h \sim 4$ ), in satisfactory agreement with the experimental data [8]; see Fig. 3.

The numerical simulations also predict a critical capillary number  $Ca \sim 0.0125$ , which is in good agreement with experimental observations [8, 10] (see Fig. 3). It is worth noting that, by scanning the capillary number, we encompass a broad range of conditions associated with different values of the physical properties, such as dynamic viscosity and surface tension, as well as operational parameters, such as the flow rate.

Figure 4 collects the main results of the present analysis. In Fig. 4(a), we show a time sequence of the pressure field from the focusing stage [(1), (2)] to the pinching (3) and finally breakup (4). This sequence unveils the following picture: The continuous phase flows back from the external reservoir to the confined microchannel (focusing stage) and the flowing jet ruptures as a consequence of the striction induced by such backflow. Note that the rupture is driven by the negative curvature, which develops in the striction region (pinching stage).

In Fig. 4(b), we show the magnitude of the flow field, scaled with the inlet velocity. In Figs. 4(b)(1) and 4(b)(2), the build-up of a significant backflow is apparent, amounting to about three times the inlet velocity. As the pinching progresses, the backflow speed decreases, due to the enlarged section available to the continuum phase. At breakup time, a very localized burst is observed, signaling the rupture of the jet. In Fig. 4(e), we zoom into the structure of the droplet and associated flow field at

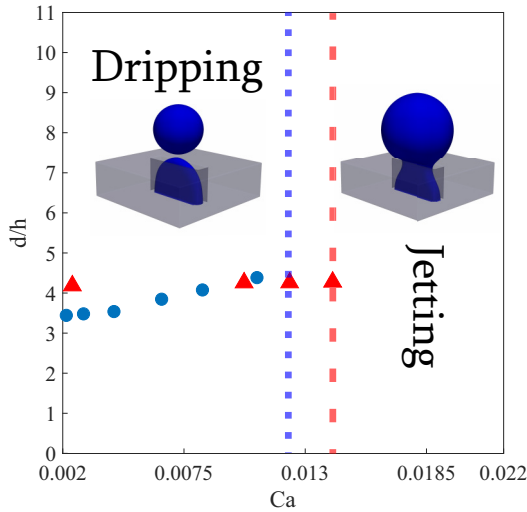


FIG. 3. Dimensionless droplet diameter ( $d/h$ ) vs the capillary number for a nozzle aspect ratio  $h/w = 1/5$ . The dots are the normalized droplet diameters predicted by the numerical simulations, while the triangles stand for the experimental values of the normalized diameters. In the dripping region, for  $Ca$  between 0.002 and  $\mathcal{O}(10^{-2})$ , the average value of the droplet diameter is  $\sim 540 \mu\text{m}$  ( $d/h \sim 4$ ). The vertical dashed (experimental) and dotted (numerical) lines denote the critical capillary numbers which mark the dripping to jetting transition.

breakup time. This figure clearly shows the re-entrant motion of the jet, accompanied by the rapid acceleration of the newborn droplet.

In Fig. 4(c), we show the time sequence of the vorticity field, in units of  $U/h$ . This sequence displays a typical elongational flow structure, especially in Fig. 4(c)(3), which stretches the jet until rupture.

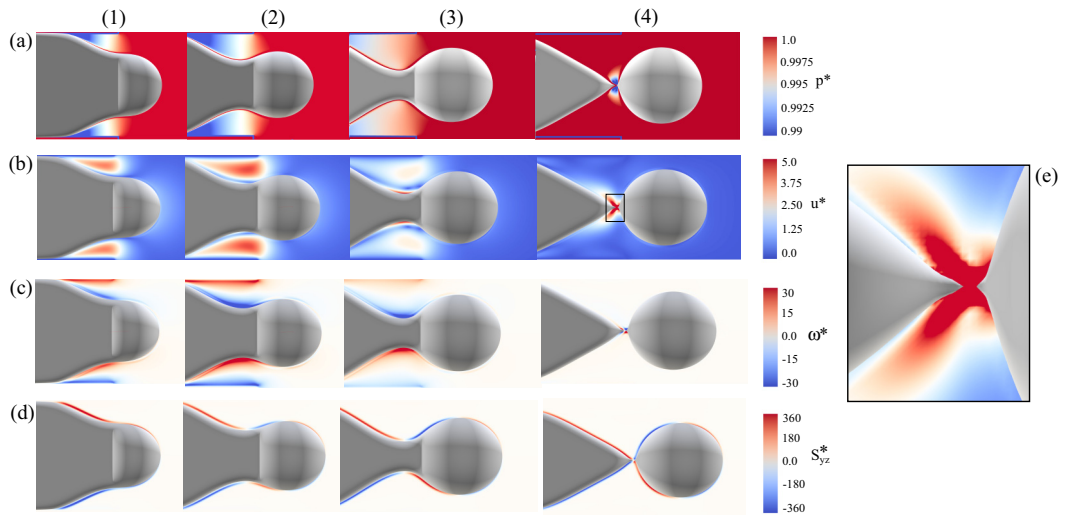


FIG. 4. (a) Pressure ( $p^*$ ), (b) velocity ( $u^*$ ), (c) vorticity ( $\omega^*$ ), and (d) stress fields ( $S_{yz}^*$ ), in a  $y$ - $z$  midplane taken between the two walls separated by  $h$ , from the focusing stage [(1), (2)] to the pinching (3) and finally breakup (4). (e) Enlargement of the droplet structure and associated flow field at breakup time. In this simulation,  $Ca = 0.003$  and  $h/w = 1/5$ .

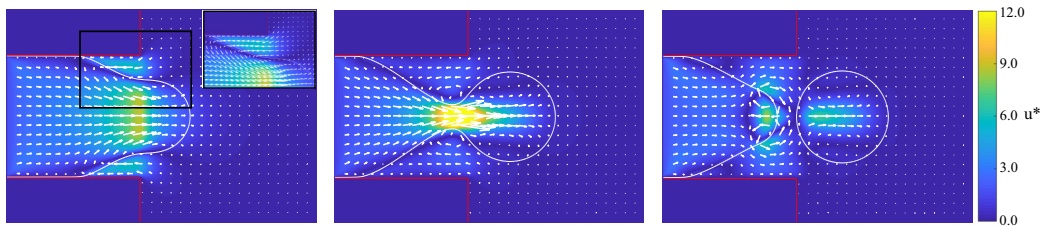


FIG. 5. Normalized velocity magnitude and vector field in the dripping nozzle. The counterflow in the continuous phase within the nozzle is clearly evidenced by the quiver plot. The solid white line identifies the interface between the continuous and the dispersed phase while the red line denotes the walls of the nozzle. The inset in the leftmost panel highlights the backflow occurring inside the nozzle.

Finally, in Fig. 4(d), we show the component of the stress field in the  $yz$  midplane, in units of  $U/h$ . The sequence shows that the stress field is highly localized around the oil-water interface, with a null point right at the pinch position [27]. The present analysis is in line with previous studies [28], in which the breakup is not interpreted as due to a plateau-Rayleigh instability [29] but rather to the backflow of the continuum phase, triggered by the adverse pressure gradient which arises in correspondence with the focusing of the water jet. We wish to emphasize that our analysis is fully dynamic and three dimensional; i.e., it does not rely on any quasistatic assumption [7] or on any axial symmetry of the flow [30].

*Dripping to jetting transition.* Most experimental studies of step emulsification report a dripping to jetting transition above a critical capillary number  $Ca_{\text{crit}} \sim \mathcal{O}(10^{-2})$  [1,8,10]. However, the underlying mechanisms behind such transition are still under investigation. Here, we wish to point out that the transition to the jetting regime is facilitated by the contribution of the dynamic pressure  $\rho_{\text{in}}u_{\text{in}}^2/2$ , with  $\rho_{\text{in}}$  and  $u_{\text{in}}$  being the local density and velocity of the dispersed phase in the pinching region. Such dynamic pressure withstands the effects of the negative curvature in the pinch region. Because of the pinching effect, the local flow speed within the dispersed phase significantly exceeds the inlet velocity. Hence, the local capillary number attains larger values, of the order of 0.1–1, whenever the nominal capillary number of the dispersed phase reaches its critical value around 0.01. Note that the nominal capillary number is computed with the imposed velocity at the inlet.

The local acceleration of the flow field inside the pinch region is clearly visible in Fig. 5, which reports the flow field inside the neck region of the dispersed phase.

As pinching progresses in time, the flow speed inside the pinching region grows accordingly, so that, at some point, inertial effects can no longer be neglected.

To clarify the point, let us write the dynamic force balance under flow conditions, namely,

$$P_{\text{in}} + \rho_{\text{in}}u_{\text{in}}^2/2 = P_{\text{out}} + \rho_{\text{out}}u_{\text{out}}^2/2 - \frac{\sigma}{\delta} \quad (1)$$

where subscripts “in” and “out” refer to the neck region (see Fig. 6), inside and outside the water jet, respectively. Note that the minus sign in front of the surface tension reflects the negative curvature (see Fig. 6).

In Eq. (1),  $\delta$  is the characteristic length scale of the neck region, which is found to be smaller but comparable with the channel height  $h$ . This is plausible, because  $\delta > h$  is not feasible since the neck diameter cannot be larger than the height of the nozzle, while  $\delta \ll h$  signals the imminent breakup.

This expression shows that the inner dynamic pressure adds to the surface tension in withstanding the outer pressure. As a result, it is natural to extend the definition of capillary number so as to include the contribution of the dynamic pressure, namely,

$$K = \frac{\mu u_{\text{in}}}{\sigma + \rho u_{\text{in}}^2 \delta / 2} \equiv \frac{Ca_{\text{in}}}{1 + We_{\text{in}}}, \quad (2)$$

where we have neglected the outer velocity since  $u_{\text{out}}/u_{\text{in}} \sim \delta/w < 1$ .

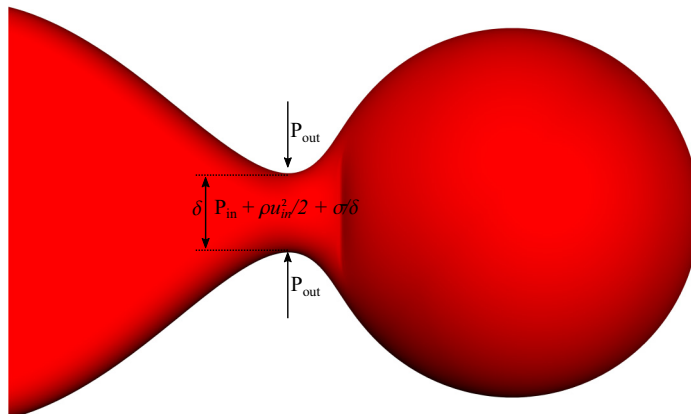


FIG. 6. Sketch of the static and dynamic pressure components in and out of the neck region.

For the case of Fig. 4, we have  $Ca_{in} = 0.015$  and  $We_{in} \sim 0.22$ , showing that the dynamic pressure is still subdominant with respect to the capillary pressure  $\sigma/\delta$ . On the other hand, in the case of jetting [see Fig. 2(c)],  $We_{in} \sim 1$ , indicating that the jetting regime is entered whenever the dynamic pressure becomes comparable or higher than the capillary pressure.

We wish to point out that since  $\delta \sim h$ ,  $Ca_{in} \sim \frac{w}{h} Ca$ , which is precisely the quantity controlling the dripping-jetting criterion discussed in Ref. [22]. In this Rapid Communication, we noted that such criterion should also take into account the contribution of dynamic pressure, which becomes dominant in the pinch region.

*Acknowledgments.* The research leading to these results has received funding from the European Research Council under the European Union’s Horizon 2020 Framework Programme (No. FP/2014-2020)/ERC Grant Agreement No. 739964 (COPMAT).

- 
- [1] S. Sugiura, M. Nakajima, N. Kumazawa, S. Iwamoto, and M. Seki, Characterization of spontaneous transformation-based droplet formation during microchannel emulsification, *J. Phys. Chem. B* **106**, 9405 (2002).
  - [2] C. Priest, S. Herminghaus, and R. Seemann, Generation of monodisperse gel emulsions in a microfluidic device, *Appl. Phys. Lett.* **88**, 024106 (2006).
  - [3] P. Garstecki, H. A. Stone, and G. M. Whitesides, Mechanism for Flow-Rate Controlled Breakup in Confined Geometries: A Route to Monodisperse Emulsions, *Phys. Rev. Lett.* **94**, 164501 (2005).
  - [4] P. Garstecki, M. J. Fuerstman, H. A. Stone, and G. M. Whitesides, Formation of droplets and bubbles in a microfluidic T-junction—scaling and mechanism of break-up, *Lab Chip* **6**, 437 (2006).
  - [5] M. Costantini, C. Colosi, P. Mozetic, J. Jaroszewicz, A. Tosato, A. Rainer, M. Trombetta, W. Świączkowski, M. Dentini, and A. Barbetta, Correlation between porous texture and cell seeding efficiency of gas foaming and microfluidic foaming scaffolds, *Mat. Sci. Eng. C* **62**, 668 (2016).
  - [6] S. L. Anna, N. Bontoux, and H. A. Stone, Formation of dispersions using “flow focusing” in microchannels, *Appl. Phys. Lett.* **82**, 364 (2003).
  - [7] R. Dangla, E. Fradet, Y. Lopez, and C. N. Baroud, The physical mechanisms of step emulsification, *J. Phys. D* **46**, 114003 (2013).
  - [8] E. Stolovicki, R. Ziblat, and D. A. Weitz, Throughput enhancement of parallel step emulsifier devices by shear-free and efficient nozzle clearance, *Lab Chip* **18**, 132 (2018).
  - [9] A. Ofner, D. G. Moore, P. A. Rühs, P. Schwendimann, M. Eggersdorfer, E. Amstad, D. A. Weitz, and A. R. Studart, High-throughput step emulsification for the production of functional materials using a glass microfluidic device, *Macromol. Chem. Phys.* **218**, 1600472 (2017).

- [10] N. Mittal, C. Cohen, J. Bibette, and N. Bremond, Dynamics of step-emulsification: From a single to a collection of emulsion droplet generators, *Phys. Fluids* **26**, 082109 (2014).
- [11] A. Montessori, M. Lauricella, M. La Rocca, S. Succi, E. Stolovicki, R. Ziblat, and D. Weitz, Regularized lattice Boltzmann multicomponent models for low capillary and Reynolds microfluidics flows, *Comput. Fluids* **167**, 33 (2018).
- [12] F. J. Higuera, S. Succi, and R. Benzi, Lattice gas dynamics with enhanced collisions, *EPL* **9**, 345 (1989).
- [13] A. Montessori, P. Prestininzi, M. La Rocca, and S. Succi, Lattice Boltzmann approach for complex nonequilibrium flows, *Phys. Rev. E* **92**, 043308 (2015).
- [14] R. Benzi, M. Sbragaglia, S. Succi, M. Bernaschi, and S. Chibbaro, Mesoscopic lattice Boltzmann modeling of soft-glassy systems: Theory and simulations, *J. Chem. Phys.* **131**, 104903 (2009).
- [15] S. Succi, *The Lattice Boltzmann Equation: For Complex States of Flowing Matter* (Oxford University Press, Oxford, UK, 2018).
- [16] S. Leclaire, M. Reggio, and J.-Y. Trépanier, Numerical evaluation of two recoloring operators for an immiscible two-phase flow lattice Boltzmann model, *Appl. Math. Model.* **36**, 2237 (2012).
- [17] T. Reis and T. N. Phillips, Lattice Boltzmann model for simulating immiscible two-phase flows, *J. Phys. A: Math. Theor.* **40**, 4033 (2007).
- [18] See Supplemental Material at <http://link.aps.org/supplemental/10.1103/PhysRevFluids.3.072202> for a detailed description of the numerical model employed [19–21].
- [19] S. Leclaire, M. Reggio, and J.-Y. Trépanier, Isotropic color gradient for simulating very high-density ratios with a two-phase flow lattice Boltzmann model, *Comput. Fluids* **48**, 98 (2011).
- [20] A. Montessori, G. Falcucci, P. Prestininzi, M. La Rocca, and S. Succi, Regularized lattice Bhatnagar-Gross-Krook model for two- and three-dimensional cavity flow simulations, *Phys. Rev. E* **89**, 053317 (2014).
- [21] R. Zhang, X. Shan, and H. Chen, Efficient kinetic method for fluid simulation beyond the Navier-Stokes equation, *Phys. Rev. E* **74**, 046703 (2006).
- [22] Z. Li, A. M. Leshansky, L. M. Pismen, and P. Tabeling, Step-emulsification in a microfluidic device, *Lab Chip* **15**, 1023 (2015).
- [23] I. Kobayashi, S. Mukataka, and M. Nakajima, Effects of type and physical properties of oil phase on oil-in-water emulsion droplet formation in straight-through microchannel emulsification, experimental and CFD studies, *Langmuir* **21**, 5722 (2005).
- [24] M. Stoffel, S. Wahl, E. Lorenceau, R. Höhler, B. Mercier, and D. E. Angelescu, Bubble Production Mechanism in a Microfluidic Foam Generator, *Phys. Rev. Lett.* **108**, 198302 (2012).
- [25] K. van Dijke, I. Kobayashi, K. Schroën, K. Uemura, M. Nakajima, and R. Boom, Effect of viscosities of dispersed and continuous phases in microchannel oil-in-water emulsification, *Microfluid. Nanofluid.* **9**, 77 (2010).
- [26] G. T. Vladisljević, I. Kobayashi, and M. Nakajima, Effect of dispersed phase viscosity on maximum droplet generation frequency in microchannel emulsification using asymmetric straight-through channels, *Microfluid. Nanofluid.* **10**, 1199 (2011).
- [27] J. Eggers, Universal Pinching of 3D Axisymmetric Free-Surface Flow, *Phys. Rev. Lett.* **71**, 3458 (1993).
- [28] V. van Steijn, C. R. Kleijn, and M. T. Kreutzer, Flows Around Confined Bubbles and Their Importance in Triggering Pinch-Off, *Phys. Rev. Lett.* **103**, 214501 (2009).
- [29] J. Eggers and E. Villermaux, Physics of liquid jets, *Rep. Prog. Phys.* **71**, 036601 (2008).
- [30] I. Chakraborty, J. Ricouvier, P. Yazhgur, P. Tabeling, and A. M. Leshansky, Microfluidic step-emulsification in axisymmetric geometry, *Lab Chip* **17**, 3609 (2017).